forests

MDPI

Article

Multi-Model Estimation of Forest Canopy Closure by Using Red Edge Bands Based on Sentinel-2 Images

Yiying Hua and Xuesheng Zhao *

College of Geoscience and Surveying Engineering, China University of Mining and Technology-Beijing, Beijing 100083, China; bqt2100205067@student.cumtb.edu.cn
* Correspondence: zxs@cumtb.edu.cn

Abstract: In remote sensing, red edge bands are important indicators for monitoring vegetation growth. To examine the application potential of red edge bands in forest canopy closure estimation, three types of commonly used models—empirical statistical models (multiple stepwise regression (MSR)), machine learning models (back propagation neural network (BPNN)) and physical models (Li–Strahler geometric-optical (Li–Strahler GO) models)—were constructed and verified based on Sentinel-2 data, DEM data and measured data. In addition, we set up a comparative experiment without red edge bands. The relative error (E_R) values of the BPNN model, MSR model, and Li–Strahler GO model with red edge bands were 16.97%, 20.76% and 24.83%, respectively. The validation accuracy measures of these models were higher than those of comparison models. For comparative experiments, the E_R values of the MSR, Li–Strahler GO and BPNN models were increased by 13.07%, 4% and 1.22%, respectively. The experimental results demonstrate that red edge bands can effectively improve the accuracy of forest canopy closure estimation models to varying degrees. These findings provide a reference for modeling and estimating forest canopy closure using red edge bands based on Sentinel-2 images.

Keywords: red edge vegetation index; feature selection; multiple stepwise regression; back propagation neural network; geometric-optical model

check for updates

Citation: Hua, Y.; Zhao, X. Multi-Model Estimation of Forest Canopy Closure by Using Red Edge Bands Based on Sentinel-2 Images. *Forests* **2021**, *12*, 1768. https://doi.org/10.3390/f12121768

Academic Editor: Steven L. Petersen

Received: 1 November 2021
Accepted: 12 December 2021
Published: 14 December 2021

1. Introduction

Forest canopy closure (CC), an essential parameter of forest structure and the forest environment, is defined as the ratio between the total shadow area projected on the ground by direct sunlight and the total area of the forest [1]. CC ranges from 0 to 1. If the canopy completely covers the ground and forms a state of complete CC, the CC value is 1, whereas, in contrast, if there is no forest cover on the ground, the CC is 0. CC is widely used in forest resource inventory, forest quality evaluation, landscape construction and other fields [2–4]. In forest management, CC is a significant basis for determining forest and sub-compartment divisions, as well as serving as an important indicator for determining tending and cutting intensity. In landscape construction, CC is a basic ecological factor that has a significant influence on multiple forest parameters, including canopy interception, throughfall and forest illuminance. On the basis of an analysis of the CC of undergrowth vegetation, we can effectively determine the species and quantity of undergrowth vegetation, which facilitates more effective management of the understory vegetation landscape in line with ecological function [5,6]. CC is also an important parameter with respect to the estimation of aboveground biomass [7,8], and more accurate estimates obtained based on CC can contribute to the management of forests with regard to wildlife habitats. Consequently, the effective inversion and monitoring of forest CC can facilitate the accurate evaluation of forest benefits and thus better serve forest resource monitoring and national forest ecological security and timber strategies.

Field collection of CC data is typically time-consuming and laborious, and it is difficult to monitor CC at a regional scale. With the rapid development of earth observation tech-

nology, remote sensing has emerged as an economic, convenient and effective approach for estimating forest CC. Nowadays, the commonly used remote sensing data are Landsat multi-spectral series, Hyperion hyperspectral series, synthetic-aperture radar (SAR), and light detection and ranging (LiDAR) data [9–11]. On the basis of different remote sensing data sources, researchers have evaluated the efficacy of different estimation models with respect to measuring forest CC. In this regard, methods that involve inversing CC using optical remote sensing data can be roughly classified into the following three categories: traditional statistical methods, machine learning methods based on data mining and physical modeling methods. This study investigated some previous research on CC estimation models based on multispectral data. The data source, study area, experimental method and accuracy measures are shown in Table 1. Researchers extracted the spectrum features, vegetation indices, texture features and other characteristic variables to monitor CC in different ways and obtained results with good accuracy.

Table 1. Accuracy of CC estimation models for different multi-spectral remote sensing data sources.

Data	Resolution	Study Area	Modeling Approach	R^2	RMSE	References
SPOT-5	10 m	Northeast Minnesota	Statistical model (PLS regression)	0.68	0.06	Wolter et al. (2009) [12]
GF-1	8 m	Qingdao City, China	Statistical model (improved Multiple linear regression)	0.651	0.023	Chen et al. (2019) [13]
GF-1	8 m	Xinjiang Province, China	Statistical model (MSR model)	0.692	0.085	Liu Saisai et al. (2020) [14]
Landsat 8	30 m	Southern Finland	Machine learning (generalized additive model)	0.7	0.1	Korhonen et al. (2011) [15]
Landsat 8	30 m	Republic of Zambia	Machine learning (K-NN algorithm)		0.13	Halperin et al. (2016) [16]
RapidEye	5 m	Republic of Zambia	Machine learning (K-NN algorithm)		0.11	Halperin et al. (2016) [16]
GF-1	8 m	Karakqin Banner, China	Machine learning (generalized additive model)	0.76	0.063	Li et al. (2020) [17]
GF-1	8 m	Xinjiang Province, China	Machine learning (BPNN)	0.713	0.082	Liu Saisai et al. (2020) [14]
GF-2	4 m	Genhe City, China	Machine learning (support vector machine)	0.65	0.12	Sun Shanshan et al. (2019) [18]
UAV	0.15 m	Zhejiang Province, China	Physical model (Li–Strahler geometric-optical model)	0.63	0.006	Wang Cong et al. (2015) [19]
Landsat 5	30 m	Anshan City, China	Physical model (mixed pixel decomposition)	0.694	0.158	Tian Haijing et al. (2013) [20]

In recent years, many scholars have discussed the application of red edge bands in different fields of remote sensing. Kang Yupeng and colleagues [21] used different types of red edge features based on GF-6 data to classify crops and analyzed the impact of different red edge features on crop classification. They extracted the spectrum features, texture features and vegetation indices of red edge bands, then screened out these features and evaluated the importance of all features. Finally, they used a random forest algorithm to classify crops. The results showed that the spectrum features, texture features and red edge vegetation index can improve the accuracy of crop classification to different degrees. Similarly, Kim Hyun-OK and colleagues [22] also studied the application potential of red edge bands in the field of crop classification. They classified Korean rice fields based on RapidEye satellite data and evaluated the accuracy of classified results. The experimental results demonstrated that the spectrum information of red edge bands is more useful than texture features, which can effectively improve the classification accuracy of rice crops. Meanwhile, some scholars have also explored red edge bands in the field of land use/land cover. Forkuor [23] used a random forest algorithm, a random gradient enhancement algorithm and a support vector machine to explore the synergy of Sentinel-2 and Landsat-8 data in the field of land use/land cover, drawing the conclusion that the experiment using

red edge bands alone obtained higher precision results than that of Landsat-8 and other Sentinel-2 bands. Kaplan [24] used a support vector machine learning classifier to analyze different wetland data sets based on Sentinel-2 red edge bands and Sentinel-1 radar bands. The results showed that the red edge bands had a significant impact on the categories of wetland which have dense, swamp-like vegetation. Griffiths and colleagues [25] obtained nationwide crop categories and land cover maps after processing and analyzing Sentinel-2 and Landsat-8 data. The experiment concluded that Sentinel-2 and Landsat-8 data have the application potential to evaluate large-area agriculture and land cover in detail, the red edge bands being capable of improving the classification accuracy of most categories of crops.

In addition, some scholars have applied red edge information to evaluation models of aboveground biomass and most of them have obtained models with better accuracy. Ren and colleagues [26] took the desert grassland of Inner Mongolia in China as a research area and used the area of a red edge reflectance curve to retrieve its aboveground biomass. The experiment showed that the red edge reflectance curve area method was a practical and suitable approach to complement the existing estimation method for green aboveground biomass in arid and semi-arid areas. Adam and colleagues [27] extracted red edge bands and calculated red edge vegetation indices based on WorldView-2 images to explore the application potential of red edge bands in the biomass inversion of densely vegetated wetlands. They used random forest algorithms to predict biomass, and the results showed that the vegetation indices calculated by red edge bands had higher accuracy than traditional spectral bands. Sibanda [28] explored the robustness of different models that integrated texture features and red edge information to predict aboveground biomass of grassland under different levels of management measures (grass burning, mowing and fertilization treatments at timely intervals). They constructed the sparse partial least squares regression algorithm based on WorldView-3 images and evaluated the accuracy of results. Experimental data indicated that red edge vegetation indices can improve the estimation accuracy of grassland biomass, and the method which combined texture features and red edge indices promised to assist in complex grassland management. The red edge bands were also widely used in research on forests, such as estimating forest leaf area index [29,30], monitoring vegetation health [31,32], predicting forest carbon stocks [33,34], etc.

Red edge bands are the area where the reflectance of vegetation changes rapidly near the junction with red light in the near-infrared band. Red edge is closely related to various physical and chemical parameters of vegetation. Researchers can use red edge to better describe the pigment state and health status of plants. The spectrum features of red edge bands and red edge vegetation indices are ideal tools for investigating vegetation states. Therefore, red edge bands have found increasing application in crop extraction, land use classification, aboveground biomass estimation and other fields. However, when searching relevant papers, the authors did not find any research exploring the application potential of red edge bands in estimating forest CC. Accordingly, in this study, we constructed a statistical model (multiple stepwise regression (MSR)), a machine learning model (back propagation neural network (BPNN)), and a physical model (Li–Strahler geometrical-optical (Li–Strahler GO)) based on Sentinel-2 data and field-measured data to estimate the CC of our study area in Chifeng City, Inner Mongolia Autonomous Region, China. We focused, in particular, on the application potential of red edge bands in forest CC estimation, and thereby provide a reference for estimating forest canopy density parameters based on different remote sensing data sources.

2. Materials and Methods

2.1. Study Area

The study area (116°21′07′′–120°58′52′′ E and 41°17′10′′–45°24′15′′ N) is located in Chifeng City, Inner Mongolia Autonomous Region, China, and includes Chifeng Municipal District, Karakqin Banner, Aohan Banner and Ningcheng County (Figure 1). The area, which has a total coverage of 14,431 km^2, lies at the intersection of the three provinces of

Mongolia, Hebei and Liaoning and has a population of 2,353,800. Chifeng is located within the transition zone from the Mongolian Plateau to the Liaohe Plain, which is characterized by a complex and diverse terrain. The study area is mainly composed of low hills, medium–high mountains, and valley plains, with altitudes ranging from approximately 500 to 2067 m. It lies within a temperate semi-arid continental monsoon climate zone, with an annual average temperature of 0–7 °C, an annual average precipitation of 381 mm, and more than 2700 h of sunshine each year. The predominant tree species in the study area include *Larix gmelinii*, *Pinus tabuliformis*, *Betula platyphylla*, *Populus davidiana* and *Quercus mongolica*.

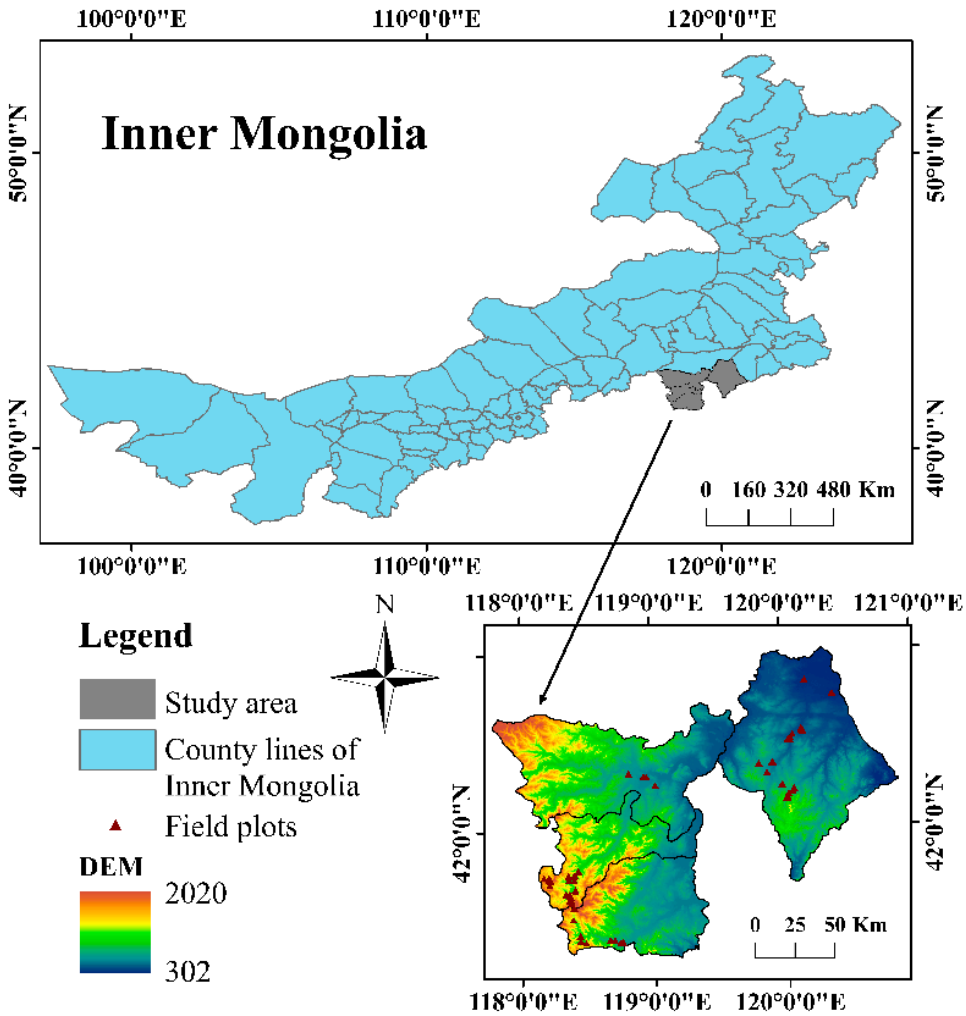

Figure 1. Overview of the study area and distribution of sampling sites.

2.2. Data

2.2.1. Remote Sensing Data

The Sentinel-2 system comprises two satellites, 2A and 2B, which were launched in June 2015 and March 2017, respectively. The satellites carry a multispectral imager (MSI), which covers 13 spectral bands with ground resolutions of 10, 20 and 60 m. Satellite images can be freely downloaded from the ESA data-sharing website (https://scihub.copernicus.eu/) (accessed on 23 June 2020). The product level is L1C, which indicates that the product has undergone geometric and radiometric corrections. For the purposes of the present study, we selected images that had been obtained at an appropriate time with little cloud cover (Table 2). We initially used SNAP software to perform atmospheric corrections and outputted blue, green, red, red edge, near-infrared and short-wave infrared bands. ENVI software was then used to complete the layer stacking step, and the pre-processed

remote sensing images were subjected to a supervised classification to extract the area of forest land within the study region. The accuracy of the classification results was verified by comparison with the measured data, which indicated that the overall accuracy of the classification reached 95%, meeting the requirements of this study.

Table 2. Parameter information for Sentinel-2 remote sensing images of the study area.

Number	Imaging Time	Tile ID	Cloud Cover (%)	Mean Solar Zenith Angle (°)	Mean Solar Azimuth Angle (°)
1	26 July 2019	T51TUG	0.0	26.349	143.380
2	31 July 2019	T50TQM	0.018	27.865	142.449
3	2 September 2019	T50TPL	0.011	35.423	154.654
4	5 September 2019	T50TNN	0.047	37.712	158.487
5	7 September 2019	T50TNM	0.179	38.254	154.894
6	22 September 2019	T50TQN	0.0	43.619	163.009
7	22 September 2019	T50TPN	0.0	43.917	161.313
8	22 September 2019	T50TPM	0.0	43.057	161.055

SRTM DEM data has the characteristics of wide coverage, large data collection and high accuracy. In this research, we downloaded the SRTM_60_04.zip and SRTM_61_04.zip of SRTM1 data with 30 m resolution, then the DEM data of the study area was obtained after splicing and clipping these data (Figure 1).

2.2.2. Field Data

Measurements of CC in the study area were obtained between 2 September and 6 September 2019. A total of seventy-one 30 m × 30 m square quadrats were established across the study area, the distribution of which is shown in Figure 1. Due to the large size of the study area, sample plots should be set up as far as possible in places with different CC degrees. CC measurements were obtained using the line transects and canopy analysis instrument methods. For the line transects method, the sampling points were systematically arranged according to a certain horizontal spacing in the sample plots and then we looked straight up at the crown at each sampling point. The CC of the plot was obtained by dividing the number of shaded points by the total number of points. For the canopy analysis instrument method, we used an LAI-2200 canopy analyzer to calculate the CC by measuring the proportion of sky visible beneath the canopy. The instrument automatically recorded the data received by optical sensor by measuring the changes of light intensity in different observation directions inside and outside the canopy of trees in the sample plots, then performed scattering correction and parameter calculation on the data. Finally, the canopy parameters were obtained based on the radiative transfer model. LAI-2200 can be used to analyze canopy porosity, and canopy closure can be obtained from 1 minus porosity.

The field data were statistically described, and the frequency distribution is shown in Figure 2. The measured maximum value is 0.96, the minimum value is 0.2 and the average value is 0.67. Among them, the sample plots with CC of 0.2–0.4 (excluding 0.4) account for 16.9% of the total sample plots, the sample plots with CC of 0.4–0.7 (excluding 0.7) account for 28.17%, while the sample plots with CC of 0.7–1 account for 54.93%.

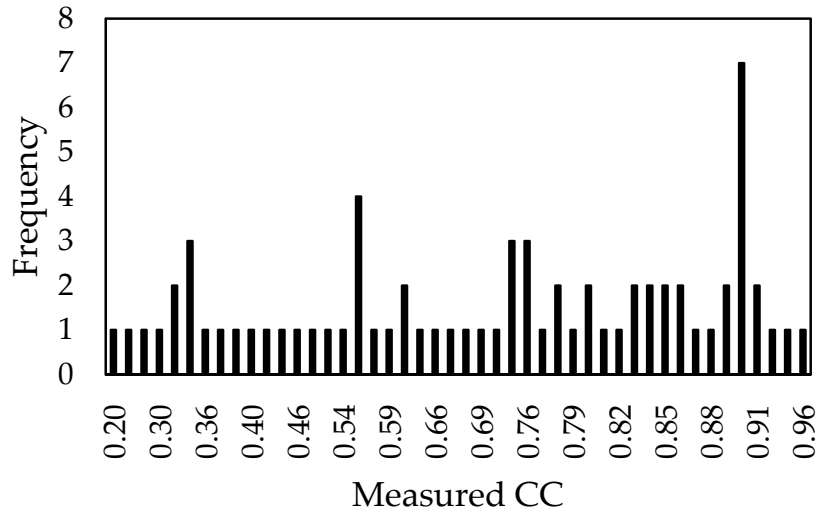

Figure 2. Measured CC frequency distribution diagram.

2.3. Methods

For the purposes of exploring the application potential of red edge bands in the construction of the CC estimation model, we selected multiple stepwise regression (MSR), back propagation neural network (BPNN) and Li–Strahler geometric-optical (Li–Strahler GO) models as representative statistical, machine learning and physical models, respectively. When using the MSR and BPNN models, the Sentinel-2 images and DEM data were used to extract the feature factors, combined with 70% of field-measured CC data to construct the model. The remaining 30% of the measured CC data was used to validate the accuracy of the models. The Li–Strahler GO model constructed in this study performed mixed pixel decomposition of all images scene by scene to obtain an endmember abundance map of the sunlit background as an input parameter of the model. Other model parameters (mean solar zenith angle, mean solar azimuth angle, mean observed azimuth angle, mean observed zenith angle, average tree height and average crown radius) were obtained from the measured data and image information. Using this information, the CC of the study area was obtained and the accuracy of the model was verified using all field-measured data.

2.3.1. Remote Sensing Variable Extraction

Based on procedures described in previous studies [17,35,36], we extracted five types of characteristic variables, namely, spectrum feature, vegetation index, red edge index, texture feature and terrain factor, the details of which are shown in Table 3. The reflectance of thirteen bands of the Sentinel-2 MSI images was extracted as the spectral characteristics. We used the Band Math tool from the ENVI software to extract the vegetation indices and red edge indices, and a co-occurrence measures tool based on second-order probability statistics was used to extract eight different texture features from the thirteen bands. Moreover, we used the spatial analyst extension of ArcGIS software to extract the terrain factors.

Table 3. Descriptions of the different feature sets.

Group	Features Variables	Description	Author and Age
Spectrum features	B2	Blue band	
	B3	Green band	
	B4	Red band	
	B5	Red edge 1 band	
	B6	Red edge 2 band	
	B7	Red edge 3 band	
	B8	NIR band	
	B8A	Narrow NIR band	
	B11	SWIR1 band	
	B12	SWIR2 band	
Vegetation indices without red edge	Enhanced vegetation index (EVI)	$2.5 \times ((B8A - B4)/(B8A + 6 \times B4 - 7.5 \times B2 + 0.5))$	Huete et al. (2002)
	Ratio vegetation index (RVI)	$B8A/B4$	Pearson et al. (1972)
	Difference vegetation index (DVI)	$B8A - B4$	Richardson et al. (1977)
	Normalized difference vegetation index (NDVI)	$(B8A - B4)/(B8A + B4)$	Rouse et al. (1974)
	Soil-adjusted vegetation index (SAVI)	$\frac{B8A-B4}{B8A+B4-0.5} \times (1 \times 0.5)$	Huete et al. (1988)
	Modified soil-adjusted vegetation index (MSAVI)	$\frac{(2\times B8A+1)-\sqrt{(2\times B8A+1)^2-8\times(B8A-B4)}}{2}$	Qi et al. (1994)
Red edge indices	Red edge chlorophyll index (CIre)	$B8A/B5 - 1$	Gitelson et al. (2003)
	Red edge simple ratio index1 (SRre1)	$B8A/B5$	Sims and Gamon (2002)
	Red edge simple ratio index2 (SRre2)	$B5/B4$	Zarco-Tejada et al. (2013)
	Modified simple ratio red edge narrow (MSRren)	$\frac{B8A/B5-1}{\sqrt{B8A/B5+1}}$	Chen et al. (1996)
	Red edge-NIR NDVI1 (NDVIre1)	$(B8A - B5)/(B8A + B5)$	Gitelson and Merzlyak (1997)
	Red edge-NIR NDVI2 (NDVIre2)	$(B8A - B6)/(B8A + B6)$	
	Red edge-NIR NDVI3 (NDVIre3)	$(B8A - B7)/(B8A + B7)$	
Texture features	Mean (Mea)	The mean of the grayscale co-occurrence matrix;	
	Variance (Var)	The variance of the grayscale co-occurrence matrix;	
	Homogeneity (Hom)	Measures the local variation of image texture, and the larger the value is, the more uniform the image is;	
	Contrast (Con)	Reflects the depth of texture; texture depth image clear;	
	Dissimilarity (Dis)	Measures local change and local contrast; the greater the value, the greater the comparability;	
	Entropy (Ent)	Measures the amount of information in an image	
	Second Moment (SM)	Reflects the uniformity of image gray distribution and texture thickness;	
	Correlation (Cor)	Reflects the local grayscale correlation in the image;	
Terrain factors	Slope	Identifies the slope from each cell of a raster surface;	
	Aspect	Identifies the downslope direction of the maximum rate of change in value from each cell to its neighbors;	
	Elevation	The distance from the absolute base plane of a point along the plumb line	
	Curvature	Measures the bending and undulating state of the earth's surface	
	Plan_Curve	Reflects the change rate of aspect	
	Profile_Curve	Reflects the change rate of slope	

In the present study, we extracted an excessive number of characteristic factors, and if all these factors had been used in modeling, it would invariably have led to a "dimensional disaster", thereby adding to the complexity of model calculation and reducing the practicality of the modeling process [37]. Therefore, to avoid this problem, we initially screened the characteristic factors prior to modeling, on the basis of which we selected those features that were relatively independent and highly correlated with CC for modeling purposes.

2.3.2. Canopy Closure Estimation Models

Multiple Stepwise Regression (MSR) Model

MSR is a method that can be used to select variables and establish an optimal regression equation [38]. The principle underlying its application is based on a consideration of the significance (contribution) of all the independent variables X to the dependent variable Y. Having established this, the variables are introduced into the model one by one and an F-test is conducted to assess whether the variable can be selected as a model component. When a former explanatory variable is no longer significant due to the entry of a subsequent explanatory variable, the former variable will be removed from the regression model. The variable entry and elimination steps are repeated until there are no more qualified optional variables outside the model and no more qualified elimination variables within the model. In this study, we used IBM SPSS Statistics software to construct the MSR model, with 70% of the measured CC values being set as dependent variables and the selected characteristic factors used as independent variables. Having established the variables, the confidence interval was set to 95%. After several rounds of characteristic variable entry and elimination, the optimal regression equation was obtained.

Back Propagation Neural Network (BPNN) Model

The BPNN model is a multi-layer feedforward network trained using an error back propagation algorithm, and is currently one of the most widely used neural network models [39]. The model has good non-linear approximation abilities and can be used to construct high-precision non-linear remote sensing models. In this study, we used MATLAB to construct a BPNN model. The model parameters used included the input layer of independent variables, the number of neurons in the hidden layer, and the output layer of the dependent variables, whereas the network structure parameters included the activation function, training function and maximum number of iterations. The number of neurons in the hidden layer can be obtained using the following empirical formula:

$$h = \sqrt{m+n} + a, \tag{1}$$

where h is the number of nodes in the hidden layer, m and n are the number of nodes in the input and output layers, respectively, and a is the adjustment constant between 1 and 10. From the perspective of accuracy, we considered as few hidden layer nodes as possible.

Li–Strahler Geometric-Optical (Li–Strahler GO) Model

As the Li–Strahler GO model requires the endmember abundance of sunlit background in each pixel as an input parameter, a fully constrained mixed pixel decomposition model is initially used to extract the endmember abundance in the image of the study area.

The fully constrained mixed pixel decomposition model can be used to decompose the area percentage of different endmembers in each pixel according to certain constraints, the specific calculation of which is shown in the following formula [40]:

$$\rho_j = \sum_{i=1}^{k} \rho_{ij} s_i + e_j, i = 1, \cdots, k; j = 1, \cdots, m, \tag{2}$$

where ρ_j is the pixel value of band, j, k is the number of endmembers, m is the number of spectral bands, ρ_{ij} is the reflectivity of band j of the endmember i, s_i is the abundance of endmember i and meets the constraints $0 \leq s_i \leq 1$, $\sum_{i=1}^{k} s_i = 1$ and e_j is the residual of band j.

The Li–Strahler GO model assumes that the tree crown is oval and analyzes the geometric structure of the ground object and decomposes pixels into four endmembers (sunlit canopy (C), sunlit background (G), shadow canopy (T), and shadow background (Z)) according to the bidirectional reflectance distribution function (BRDF) [41,42]. When using this model, the surface reflectance of the remote sensing images is described as the sum of the area percentage weights of the four endmembers. The calculation is as follows:

$$K_g = e^{-\pi M[\sec\theta_i + \sec\theta_v - O(\theta_i,\theta_v,\varphi)]}, \tag{3}$$

where θ_i is the solar zenith angle, θ_v is the observation zenith angle, φ is the relative azimuth angle between the sun and the satellite, M is the mean of the tree cover index m defined as $m = \lambda r^2$, λ is the tree density and r is the average crown radius within the pixel, $\mathrm{O}(\theta_i, \theta_v, \varphi)$, and is the overlapping part of the illumination shadow and observation shadow, which is referred to as the overlap function and is calculated as follows:

$$\mathrm{O}(\theta_i, \theta_v, \varphi) = (t - \sin t \cos t)(\sec\theta_i + \sec\theta_v)/\pi, \tag{4}$$

in which

$$\cos t = h|\tan\theta_i - \tan\theta_v \cos\varphi|/r(\sec\theta_i + \sec\theta_v), t \in [0, \pi/2], \tag{5}$$

where h is the average tree height in the pixel.

The expression of M is as follows, according to Formulae (3) and (4):

$$\mathrm{M} = -\ln K_g/(\sec\theta_i + \sec\theta_v)(\pi - t + \sin t \cos t), \tag{6}$$

Accordingly, the expression of CC is as follows:

$$\mathrm{CC} = 1 - e^{-\pi M}. \tag{7}$$

2.4. Model Inspection

In this study, the decision coefficient (R^2), root mean square error (RMSE) and relative error (E_R) were selected as evaluation indices to verify these models. Normally, if the value of R^2 is higher and the value of RMSE is smaller, the fitting effect is better and the prediction ability of the model is stronger, whereas, the smaller the E_R value, the higher the estimation accuracy of the model. The mathematical formulae for each of these indices are as follows:

$$R^2 = 1 - \frac{\sum_{i=1}^{n}(y_i - x_i)^2}{\sum_{i=1}^{n}(y_i - \overline{x_i})^2}, \tag{8}$$

$$\mathrm{RMSE} = \sqrt{\frac{1}{n}\sum_{i=1}^{n}(y_i - x_i)^2}, \tag{9}$$

$$\mathrm{E}_R = \frac{x_m - y_m}{y_m} \times 100, \tag{10}$$

where y_i is the value of the training sample i, x_i is the estimated value of the training sample i, $\overline{y_i}$ is the average value of the training samples, $\overline{x_i}$ is the average value of the estimated value of the model, x_m is the estimated value of the sample m, y_m is the ground-measured value of the sample m and n is the number of samples.

3. Results

3.1. Feature Selection

In this paper, 10 spectrum features, six vegetation indices without red edge, seven red edge indices, 80 texture features and six terrain factors—a total of 109 alternative feature factors—were extracted. To eliminate the feature factors which contain redundant information and have weak correlation with dependent variables, we initially calculated the correlation coefficient matrix between CC and each characteristic factor. First, the

correlation coefficient matrix for spectrum features and CC was calculated, as shown in Table 4. It can be seen from the table that the blue band showed the highest correlation with CC and also showed a weak correlation with RE2, RE3 and NIR bands among the spectrum features, and thus we retained the blue band, green band, red band, RE1 band, SWIR1 band and SWIR2 band. Then, the correlation coefficient matrix for vegetation indices and CC was calculated as well, as shown in Table 5. Compared with other vegetation indices, the correlation between DVI and CC was weak. From the correlation coefficient matrix between DVI and other vegetation indices (Table 6), there is a significant correlation between DVI and other vegetation indices at the confidence level of 0.01. This means that there is much overlapping information between DVI and other vegetation indices, so DVI is replaceable. Therefore, the DVI variables were removed, and the feature variables of EVI, MSAVI, NDVI, RVI and SAVI were preliminarily retained. In the same way, we calculated the correlation coefficient matrix between the remaining feature variables and CC respectively, as shown in Tables 7–9.

Table 4. Correlation coefficient matrix for spectrum features and CC.

	Blue	Green	Red	RE1	RE2	RE3	NIR	NIR_narrow	SWIR1	SWIR2
Pearson correlation coefficient	−0.761 **	−0.721 **	−0.744 **	−0.684 **	−0.220	−0.088	−0.007	−0.061	−0.616 **	−0.689 **

Note: **. Significant correlation at the $p \leq 0.01$ level (bilateral).

Table 5. Correlation coefficient matrix for vegetation indices and CC.

	DVI	EVI	NDVI	RVI	SAVI	MSAVI
Pearson correlation coefficient	0.242 *	0.601 **	0.703 **	0.628 **	0.703 **	0.708 **

Note: **. Significant correlation at the $p \leq 0.01$ level (bilateral); *. Significant correlation at the $p \leq 0.05$ level (bilateral).

Table 6. Correlation coefficient matrix between DVI and other vegetation indices.

	EVI	NDVI	RVI	SAVI	MSAVI
Pearson correlation coefficient	0.549 **	0.414 **	0.441 **	0.414 **	0.405 **

Note: **. Significant correlation at the $p \leq 0.01$ level (bilateral).

Table 7. Correlation coefficient matrix for red edge vegetation indices and CC.

	CIre	SRre1	SRre2	MSRren	NDVIre1	NDVIre2	NDVIre3
Pearson correlation coefficient	0.602 **	0.602 **	0.605 **	0.622 **	0.648 **	0.323 **	−0.357 **

Note: **. Significant correlation at the $p \leq 0.01$ level (bilateral).

Table 8. Correlation coefficient matrix for terrain factor and CC.

	Slope	Aspect	Elevation	Curvature	Plan_Curve	Profile_Curve
Pearson correlation coefficient	0.414 **	0.201	0.529 **	0.051	0.049	−0.004

Note: **. Significant correlation at the $p \leq 0.01$ level (bilateral).

Table 9. Correlation coefficient matrix for texture feature and CC in each band.

	Con	Cor	Dis	Ent	Hom	Mea	SM	Var
Blue band (1)	0.047	0.043	0.072	0.127	−0.077	−0.681 **	−0.430 **	0.073
Green band (2)	−0.059	0.258 *	−0.059	−0.103	0.059	−0.741 **	0.108	−0.067
Red band (3)	−0.172	0.327 **	−0.297 *	−0.382 **	0.325 **	−0.734 **	0.380 **	−0.471 **
RE1 band (4)	−0.141	0.252 *	−0.147	−0.088	0.145	−0.691 **	0.117	−0.143
RE2 band (5)	0.200	−0.122	0.237 *	0.300 *	−0.241 *	−0.180	−0.274 *	0.230
RE3 band (6)	0.219	0.144	0.181	0.162	−0.145	−0.068	−0.123	0.225
NIR band (7)	0.182	0.284 *	0.133	−0.016	−0.091	−0.032	0.087	0.238 *
NIR_Narrow band (8)	0.422 **	−0.361 **	0.442**	0.464 **	−0.435 **	−0.064	−0.432 **	0.332 **
SWIR1 band (9)	0.190	−0.043	0.208	0.279 *	−0.200	−0.620 **	−0.249 *	0.118
SWIR2 band (10)	0.141	0.014	0.084	0.036	−0.018	−0.687 **	0.004	0.055

Note: **. Significant correlation at the $p \leq 0.01$ level (bilateral); *. Significant correlation at the $p \leq 0.05$ level (bilateral).

It can be seen from Tables 8 and 9 that the retained characteristic variables can be selected directly according to the correlation coefficient between red edge indices, terrain factors and CC. All red edge indices were retained temporarily, because the red edge indices were significantly correlated with CC at the confidence level of 0.01, whereas only slope and elevation factors were retained.

Through the correlation analysis between the texture features of each band and CC (Table 9), the texture features with weak correlation were screened out and eliminated. Eleven feature factors with significant correlation with CC at the confidence level of 0.05 and 19 feature factors with significant correlation at the confidence level of 0.01 were retained. After that, there were still a large number of texture features reserved which had redundant information. Thereby, the remaining 30 texture features with high correlations were subjected to additional screening to simplify the variables for building the model. The texture features of the RE2 and SWIR1 bands and CC are significant at the confidence level of 0.05, whereas most texture features of the red and NIR_narrow bands are significantly correlated with CC. Therefore, the correlation analysis was carried out for the remaining texture features of the RE2, SWIR1, red and NIR_narrow bands, as shown in Tables 10–13.

Table 10. Correlation coefficient matrix of texture features in red edge band 2.

	Dis5	Ent5	Hom5	SM5
Dis5	1	0.865 **	−0.984 **	−0.847 **
Ent5	0.865 **	1	−0.880 **	−0.975 **
Hom5	−0.984 **	−0.880 **	1	0.888 **
SM5	−0.847 **	−0.975 **	0.888 **	1

Note: **. Significant correlation at the $p \leq 0.01$ level (bilateral).

Table 11. Correlation coefficient matrix of texture features in short-wave infrared band 1.

	Ent9	SM9	Mea9
Ent9	1	−0.974 **	0.014
SM9	−0.974 **	1	−0.046
Mea9	0.014	−0.046	1

Note: **. Significant correlation at the $p \leq 0.01$ level (bilateral).

Table 12. Correlation coefficient matrix of texture features in red band.

	Cor3	Dis3	Ent3	Hom3	Mea3	SM3	Var3
Cor3	1	−0.663 **	−0.666 **	0.709 **	−0.297 *	0.693 **	−0.601 **
Dis3	−0.663 **	1	0.898 **	−0.990 **	0.309 **	−0.898 **	0.737 **
Ent3	−0.666 **	0.898 **	1	−0.920 **	0.351 **	−0.993 **	0.841 **
Hom3	0.709 **	−0.990 **	−0.920 **	1	−0.325 **	0.923 **	−0.766 **
Mea3	−0.297 *	0.309 **	0.351 **	−0.325 **	1	−0.348 **	0.422 **
SM3	0.693 **	−0.898 **	−0.993 **	0.923 **	−0.348 **	1	−0.821 **
Var3	−0.601 **	0.737 **	0.841 **	−0.766 **	0.422 **	−0.821 **	1

Note: **. Significant correlation at the $p \leq 0.01$ level (bilateral); *. Significant correlation at the $p \leq 0.05$ level (bilateral).

Table 13. Correlation coefficient matrix of texture features in the near-infrared narrow band.

	Con8	Cor8	Dis8	Ent8	Hom8	SM8	Var8
Con8	1	−0.291 *	0.953 **	0.740 **	−0.874 **	−0.638 **	0.783 **
Cor8	−0.291 *	1	−0.448 **	−0.562 **	0.528 **	0.633 **	−0.129
Dis8	0.953 **	−0.448 **	1	0.853 **	−0.980 **	−0.794 **	0.671 **
Ent8	0.740 **	−0.562 **	0.853 **	1	−0.886 **	−0.971 **	0.608 **
Hom8	−0.874 **	0.528 **	−0.980 **	−0.886 **	1	0.859 **	−0.567 **
SM8	−0.638 **	0.633 **	−0.794 **	−0.971 **	0.859 **	1	−0.500 **
Var8	0.783 **	−0.129	0.671 **	0.608 **	−0.567 **	−0.500 **	1

Note: **. Significant correlation at the $p \leq 0.01$ level (bilateral); *. Significant correlation at the $p \leq 0.05$ level (bilateral).

There is a strong correlation between the homogeneity, dissimilarity, entropy and second moment of red edge band 2 (Table 10). Therefore, the entropy factors with relatively good correlation with CC and significant correlation with other features were retained, and other features were eliminated. Similarly, the entropy and mean features of short-wave infrared band 1 were selected according to Table 11. From Table 12, among the texture features of red band, the homogeneity features are significantly correlated with the dissimilarity, entropy and second moment feature. So, the homogeneity feature was retained, while the correlation, mean and variance features with weak correlation were all retained temporarily. In a similar way, we chose the correlation, entropy and variance characteristics of the near-infrared (narrow) band according to Table 13.

Through the correlation analysis of all the remaining texture feature variables, it can be found that there was a strong correlation between the mean feature factors of different bands, in which the mean features of green band were significantly correlated with those of blue band, red band and red edge band 1. Therefore, in order to reduce informational redundancy, the mean feature of green band was retained. The Pearson correlation coefficient of the mean features of short-wave infrared band 1 and short-wave infrared band 2 was 0.952, which was significantly correlated at the confidence level of 0.01. Therefore, the short-wave infrared 2 factor with higher correlation with CC was retained in the two features.

Finally, there were 35 feature variables left after correlation analyses. The results are shown in Table 14.

Table 14. Summary of features after preliminary screening.

Group	Features Variables
Spectrum features	Blue, Green, Red, RE1, SWIR1, SWIR2
Vegetation indices without red edge	EVI, NDVI, RVI, SAVI, MSAVI
Red edge indices	CIre, SRre1, SRre2, MSRren, NDVIre1, NDIVre2, NDVIre3
Texture features	Slope, Elevation
Terrain factors	SM1, Cor2, Mea2, Cor3, Hom3, Var3, Cor4, Hom5, Cor7, Var7, Cor8, Var8, Ent8, Mea9, SM9

Using the feature variable selection of a random forest algorithm, the variables after preliminary screening were subjected to further analysis. Based on a Gini index, the contribution of each variable to CC was calculated and quantified. Moreover, the output results were normalized and sorted as shown in Figure 3.

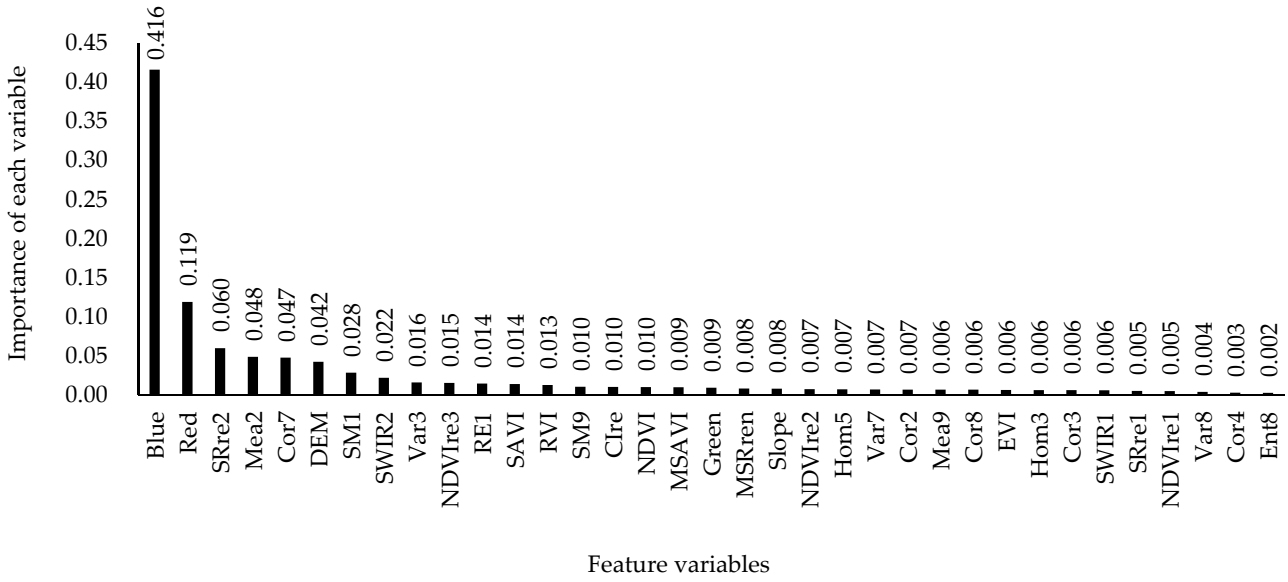

Figure 3. Importance of feature variables.

Figure 3 shows that the weights of 35 feature variables varied greatly. Among them, the importance of blue band was much higher than that of other variables, followed by the importance of red band, SRre2, Mea2 and Cor7. The importance of Ent8 was the lowest. According to the importance ranking table of whole feature variables, the sum of normalized importance weights of the first 10 feature variables was 0.813, indicating that the first 10 feature variables made the highest contribution to CC, while the contribution of the last 25 characteristic variables to CC was small. Therefore, in order to simplify the input model variables, the top 10 feature variables were selected as the model input variables, that is, the spectrum features of blue band, red band and SWIR2 band, the red edge vegetation indices (SRre2 and NDVIre3), the texture features (Mea2, Cor7, SM1 and Var3) and the terrain factor (Elevation) were selected as the input variables of the MSR model and the BPNN model.

3.2. The Modeling Results Obtained Using MSR and BPNN Models

Following multiple screening and regression, the optimal regression equation of CC was obtained using the following MSR model:

$$\mathrm{CC} = 1.178 - 0.001 \times \mathrm{Blue} + 0.018 \times \mathrm{SRre2} + 0.176 \times \mathrm{NDVIre3} - 0.199 \times \mathrm{SM1} - 0.348 \times \mathrm{Var3} \quad (11)$$

The regression equation retains five characteristic factors, namely, reflectance of blue band, red edge simple ratio index 2, red edge-NIR NDVI3, second moment texture feature of blue band, and variance texture feature of red band, whereas other features were eliminated.

When using the BPNN model, it is essential to select appropriate transfer and training functions, as well as a suitable number of hidden layer neurons. In this study, we constructed a network model with an input layer–hidden layer–output layer of 10–7–1 based on comparative experiments. The transfer function of the input layer to the hidden layer was tansig, the transfer function of the hidden layer to the output layer was purelin and the training function was trainlm.

The accuracy measures of MSR and BPNN modeling are shown in Table 15, and scatter diagrams of the modeling accuracy verification results are shown in Figure 4.

Table 15. A comparison of modeling accuracy.

Model	R^2	RMSE
MSR	0.685	0.135
BPNN	0.817	0.088

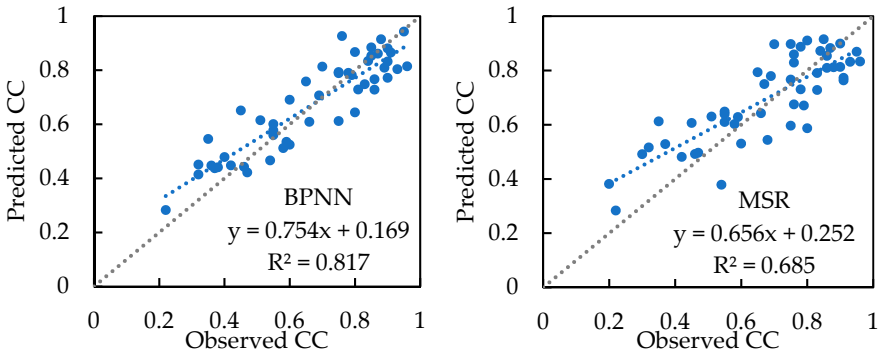

Figure 4. Scatter plots of measured values of canopy cover and estimated values of modeling points.

3.3. The Modeling Results Obtained Using Li–Strahler GO Models

To extract the abundance of endmembers, the Li–Strahler GO model was simplified to a three-component model [26], that is, the pixels in the study area comprised the sunlit canopy, sunlit background, and shadow. The minimum noise fraction was carried out for the image in the study area to eliminate noise and retain useful information. Then, the first component and the second component which contain the most useful information as X and Y axes were selected to form a two-dimensional scatter diagram. In general, the geometric positions of pure endmembers are distributed at three vertices of the triangle, while the points inside (i.e., mixed pixels) are the linear combination of three vertices. Therefore, in this study, the sample points of three vertex regions of the triangle represented in a 2D scatter diagram were selected as pure endmember sample points to extract their average spectrum. According to previous research [43–45], we analyzed the corresponding relationship between the extracted three spectral curves and the sunlit background, sunlit canopy and shadow, respectively. Finally, fully constrained mixed pixel decomposition was performed to obtain the sunlit background abundance (K_g).

The K_g maps were inputted into the model scene by scene and estimates of forest CC in the study area were accordingly obtained. Taking a scene image as an example, the input parameters are listed in Table 16. Information relating to the zenith and azimuth angles was obtained from the image header file and that for average tree height and average crown radius was obtained from the measured data.

Table 16. Input parameters of the Li–Strahler GO model used to analyze a single scene image.

Parameter	Value
Mean solar zenith angle ($\theta_i(^\circ)$)	26.38
Mean view zenith angle ($\theta_v(^\circ)$)	2.69
Mean solar azimuth angle ($\varphi_i(^\circ)$)	143.35
Mean view azimuth angle ($\varphi_v(^\circ)$)	179.51
Average tree height (h(m))	12.53
Average crown radius (r(m))	3.59

Based on the Li–Strahler GO model, we conducted CC inversion experiments using Sentinel-2 images scene by scene. All results obtained were spliced, and the forest CC results in the study area were extracted according to the forest cover area (Figure 5).

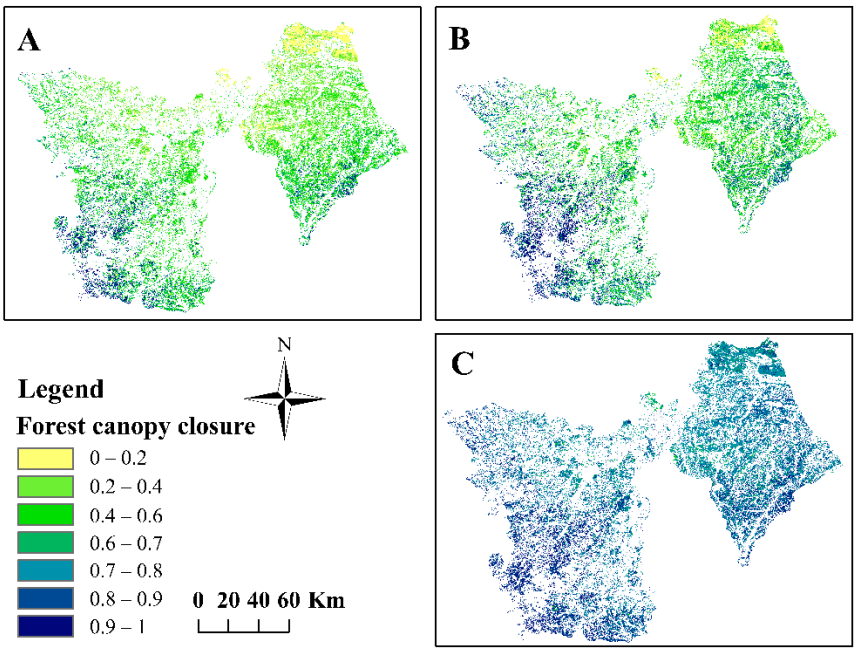

Figure 5. CC inversion results obtained using the Li–Strahler geometric-optical (**A**), multiple stepwise regression (**B**) and back propagation neural network (**C**) models.

3.4. Evaluation of the Accuracy of the Three Models

The accuracy of forest CC inversion performed by MSR and BPNN models was verified using 30% of completely independent measured data as test samples, whereas the inversion result obtained by the Li–Strahler GO model was verified using all the measured data for the sampling points. The fitting effects of the three models were compared based on an evaluation of R^2, RMSE and E_R (Table 17, Figure 6).

Table 17. A comparison of model accuracy validation.

Model	R^2	RMSE	E_R (%)
Li–Strahler GO	0.451	0.187	24.83
MSR	0.75	0.162	20.76
BPNN	0.811	0.108	16.97

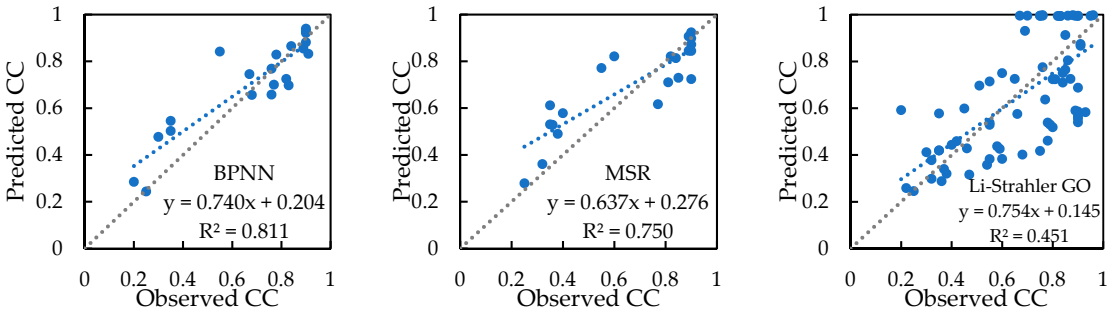

Figure 6. Scatter plot of the measured values of canopy cover and estimated values of test points.

3.5. Comparative Experiments

Multispectral images are the most common remote sensing data source used to estimate forest CC. The main reason is that these data are easy to obtain and have long time series. In this study, comparative experiments were carried out to further analyze the positive role of red edge bands in inversion models. Firstly, for MSR and BPNN models,

we constructed CC estimation models based on selected characteristic factors excluding red edge vegetation indices (i.e., using Blue, Red, Mea2, Cor7, Elevation, SM1, SWIR2, Var3 features) with 70% of measured data as modeling samples. Secondly, the synthetic images of visible bands, near-infrared bands and short-wave infrared bands of Sentinel-2 were used to retrieve forest CC in the study area based on the Li–Strahler GO model. Finally, the estimation accuracy of CC of each model without participation of red edge bands was calculated, as shown in Table 18.

Table 18. The estimation accuracy of comparative experiments.

Model	R^2	RMSE	E_R (%)
Li–Strahler GO	0.456	0.249	28.83
MSR	0.697	0.168	33.83
BPNN	0.787	0.120	18.19

4. Discussion

4.1. The Accuracy of the Three Types of Models

According to the modeling accuracy table and estimation accuracy table of models (Tables 15 and 17), it can be found that the BPNN model had the highest accuracy of both modeling and estimation, followed by the MSR model. The estimation accuracy of the Li–Strahler GO model was relatively low.

Given that the characteristic factors of the MSR and BPNN models were consistent and that we used the same number of measured sample plots, we found the inversion results and accuracy of the two models to be comparable. The reason the accuracy of the BPNN model was better than the MSR model may be because the BPNN model is a semi-empirical model based on data mining, which reduces error by continuously adjusting the network weight in the modeling process, so that the model can better establish the nonlinear relationship between data. It is more flexible and has better learning ability. However, the regression model is a parametric model, which cannot well represent nonlinear relationships. The advantage of the MSR model is its ability to intuitively reveal the influence of independent variables on dependent variables. We believe that the forest has a complex background environment, and the relationship between CC and remotely sensed data is not a simple linear relationship. Therefore, a better estimation result of CC was obtained with the BPNN model.

However, the BPNN model also has some limitations. For example, this type of model is a black box operation; we cannot quantitatively analyze the correlation between various factors and CC. Secondly, the characteristic variables of the input model affect the accuracy and stability of the model. If a large number of variables were directly inputted into the model without feature screening before modeling, "dimension disaster" and overfitting of the model would result, while the MSR model can gradually screen significant variables and eliminate irrelevant variables in the modeling process to ensure the simplicity and stability of the model. Interestingly, however, we found that both the MSR and BPNN models are characterized by a phenomenon whereby verification accuracy is higher than modeling accuracy, which indicates that the stability of the two models is insufficient and that their generalization ability is weak. We speculate that these deficiencies could be attributable to the uneven distribution of the training and test data sets, or it may be that fewer sampling sites were covered in the field investigation.

In addition, by analyzing the estimated and measured values of test samples, it was found that both the MSR and BPNN models underestimated the areas of high CC and overestimated the areas of low CC to varying degrees. For the MSR model, almost all the sample plots that measured CC less than 0.6 were overestimated, and its average overestimation was 0.21, while 53.85% of the sample plots that measured CC greater than or equal to 0.6 were underestimated. The overestimation in the low CC area of the BPNN model was significantly better than that of the MSR model. The overestimation proportion of the BPNN model with the value of sample points less than 0.6 was 77.78% and the

overestimation was only 0.03 on average, while the underestimation proportion with the value of sample points greater than or equal to 0.6 was 58.33%. With respect to the causes of underestimation, it may be that the optical remotely sensed images have signal saturation in the area with high CC, meanwhile, the sensitivity of characteristic variables extracted based on the images was reduced. In the area of low CC, there are always shrubs, grasses and other sorts of vegetation in canopy gaps, as well as soil background and other noise; as a result, the overestimation problem was serious.

Compared with the MSR and BPNN models, the validation accuracy of the Li–Strahler GO model was somewhat lower and values were generally underestimated, which may be due to the large scope of the study area. In this study, we used a scene of an image as a unit and the average value of each parameter of each unit was taken as an input parameter of the model, which accordingly resulted in a decline in model accuracy. Moreover, the terrain of the study area is complex and the angle parameters were not transformed according to terrain conditions. Consequently, it is assumed that errors in inversion results were, at least in part, associated with topographic factors. Besides, the Li–Strahler GO model is a physical model based on canopy reflectance, which is greatly affected by canopy coverage. The forest vegetation in the study area is dense, and there are sheltered and overlapping parts in the tree crown which affected the accuracy of calculating canopy shadow overlap function in the geometric-optical model, resulting in a reduction of model accuracy. At the same time, crown shape also affected the accuracy of the Li–Strahler GO model, which is a simplified model with an oval crown hypothesis. The dominant tree species in the study area are larch and *Pinus tabulaeformis*, the crown shapes of which are umbrella-like and conical, which did not meet the crown hypothesis, leading to some estimation errors.

In general, the three types of models have different advantages and disadvantages when it comes to constructing a CC estimation model with good accuracy. The MSR model can quickly estimate CC at a regional scale in a specific area with a simple and intuitive model structure. However, it is obviously affected by background noise. Moreover, this model is not universally applicable, that is, it needs to be re-modeled for different study areas. The BPNN model obtained the highest accuracy result in this study, which means it is more suitable for the mixed situation of ground objects. However, this model has some weaknesses, such as a complex structure, slow calculation speed and the need of a large number of sample data to support modeling. Compared with the first two models, the Li–Strahler GO model is widely applicable and does not require training samples while modeling. It can directly calculate forest parameters based on remotely sensed images according to a physical mechanism, which is more economical, convenient and time-saving. Although the models constructed in this paper have achieved good accuracy results, there are still some problems that need to be further explored. For example, how to obtain the input parameters with higher accuracy, how to transform the angle parameters to adapt to mountainous terrain conditions and how to improve the accuracy of the mixed pixel decomposition.

4.2. The Applicability of Red Edge Bands

As indicated in the regression equation (Formula (11)), the SRre2 and NDVIre3 calculated from red edge bands contributed to the inversion of CC. This means that red edge indices can be effectively applied to forest CC inversion models.

In order to further explore the contribution of red edge bands in different models, this study set up comparative experiments to analyze fluctuations in the accuracy of different models after excluding red edge bands and red edge vegetation indices. Comparing the accuracy results in Tables 17 and 18, it can be found that using red edge bands in modeling can effectively improve the estimation accuracy of all three types of models. The R^2 of the MSR model in the comparative experiment was lower than that of the former experiment, while RMSE was slightly higher and E_R was much higher, indicating that, under the same modeling condition, removing red edge bands would reduce the estimation accuracy of the regression model. The BPNN model in the comparative experiment also obtained a

slightly lower R^2, a slightly higher RMSE and a higher E_R, which shows that red edge bands can improve the estimation accuracy of a machine learning model as well. Last but not least, for the geometric-optical model, the R^2 of the comparative experiment was only 0.005 higher than that of the former experiment, while both RMSE and E_R were higher, indicating that red edge bands can improve the estimation accuracy of a physical model to a certain extent.

Although red edge bands have positive effects on the three types of models, the accuracy of different models was improved to different degrees. The MSR model was most affected by red edge bands and the estimation accuracy was greatly improved. Compared with the former experiment, the relative error of the comparative experiment was increased by 13.07%. Secondly, the Li–Strahler GO model showed a certain decrease in accuracy in the comparative experiment; its relative error was 4% higher than that of the former experiment. The BPNN model was least affected by red edge bands, with the estimation accuracy only reduced by 1.22% after removing red edge vegetation indices.

The reason red edge bands had different accuracy effects on different models may be that the red edge vegetation indices were important dependent variables that contributed greatly to the MSR model. Removing red edge bands and using only the remaining dependent variables cannot well explain the independent variable, so the accuracy of this model decreased significantly. The BPNN model is a nonlinear model with good robustness, so the accuracy of the BPNN model decreased the least after removing red edge bands. For the physical model, it is worth noting that the geometric-optical model is a complex model based on the mechanism of canopy reflectance, which contains several input parameters. In this study, we estimated CC based on the simplified Li–Strahler GO model, which only retained six parameters, with large uncertainties. Moreover, this kind of model always needs high-quality input parameters to ensure its accuracy; however, only the average values of tree height and crown width of sample points were used as the input parameters for all scenes of images, which caused a large number of errors. Therefore, this study only set up a simple comparative experiment for images with or without red edge bands to explore the influence of red edge bands on the geometric-optical model, which is controversial, and the mechanism of influence of red edge bands on it needs to be further investigated.

5. Conclusions

Compared with traditional methods, the use of remote sensing represents an effective approach for determining the distribution of forest canopy closure at a regional scale and thereby provides a convenient and feasible method for monitoring and managing forest resources. In this regard, red edge bands are an ideal tool for investigating vegetation status and have certain application potential with respect to forest parameter inversion. In this study, we used Sentinel-2 data to construct statistical (multiple stepwise regression), machine learning (back propagation neural network), and physical (Li–Strahler geometric-optical) models. To assess canopy closure, we introduced vegetation indices calculated from red edge bands into estimation models and analyzed their applicability. On the basis of our analysis of the accuracy of the three models, the following conclusions can be drawn:

1. Red edge bands can be used in forest canopy closure estimation models. According to the correlation coefficient matrix and the ranking results of the importance of characteristic variables, it can be seen that spectrum features are the most important features with respect to canopy closure among the five types of feature factors extracted in this study, followed by red edge vegetation indices. Moreover, the model estimation results indicate that Sentinel-2 data have potential utility with respect to the estimation of forest canopy closure based on our findings that the multiple stepwise regression model incorporating red edge indices had an R^2 value of 0.75 and a relative error value of 20.76%, whereas the back propagation neural network model incorporating red edge indices had an R^2 of 0.811 and relative error of 16.97%. In addition, the Li–Strahler geomatic optical model constructed by the synthetic images

within red edge bands showed a certain reliability as well, with a relative error value of 24.83%. Compared with comparative experiments and previous research into the construction of canopy closure estimation models based on multispectral images, this paper used the red edge indices calculated by red edge bands in the construction of the models and obtained better accuracy results.

2. Although red edge bands can effectively improve the accuracy of forest canopy closure estimation models, they have different effects on different types of models. The multiple stepwise regression model was most affected by red edge bands. Compared with the model without red edge vegetation indices, the accuracy of the multiple stepwise regression model with red edge vegetation indices improved by 13.07%, which shows that, out of the three models, red edge bands have the best adaptability and effectiveness in the multiple stepwise regression model. The second is the Li–Strahler geometric-optical model. The canopy closure result of image inversion with red edge bands was 4% higher than without red edge bands, which also shows that red edge bands can be better applied to this kind of model and can improve accuracy. Finally, red edge bands contribute the least improvement to the back propagation neural network model, and improved the model accuracy by only 1.22%.

The findings of this study can thus provide a reference for the inclusion of red edge band information in the modeling and estimation of forest canopy closure.

Author Contributions: Y.H. and X.Z. conceived and designed the experiments; Y.H. performed the experiments; Y.H. and X.Z. analyzed the data; Y.H. wrote the paper; X.Z. reviewed and edited the paper. All authors have read and agreed to the published version of the manuscript.

Funding: This research was funded by the National Natural Science Foundation of China, grant number 41930650.

Institutional Review Board Statement: Not applicable.

Informed Consent Statement: Not applicable.

Data Availability Statement: The dataset of Sentinel-2 and SRTM1 are openly available at https://scihub.copernicus.eu/ (accessed on 23 June 2020), https://earthexplorer.usgs.gov/ (accessed on 23 December 2019).

Conflicts of Interest: The authors declare no conflict of interest.

References

1. Jennings, S. Assessing Forest Canopies and Understorey Illumination: Canopy Closure, Canopy Cover and Other Measures. *Forestry* **1999**, *72*, 59–74. [CrossRef]
2. Wilkinson, M.; Eaton, E.L.; Morison, J.I.L. Can Upward-Facing Digital Camera Images Be Used for Remote Monitoring of Forest Phenology? *For. Int. J. For. Res.* **2018**, *91*, 217–224. [CrossRef]
3. Lof, M.; Karlsson, M.; Sonesson, K.; Welander, T.N.; Collet, C. Growth and Mortality in Underplanted Tree Seedlings in Response to Variations in Canopy Closure of Norway Spruce Stands. *Forestry* **2007**, *80*, 371–383. [CrossRef]
4. Buskey, T.M.; Maloney, M.E.; Chapman, J.I.; McEwan, R.W. Herb-Layer Dynamics in an Old-Growth Forest: Vegetation–Environment Relationships and Response to Invasion-Related Perturbations. *Forests* **2020**, *11*, 1069. [CrossRef]
5. Caselli, M.; Urretavizcaya, M.F.; Loguercio, G.Á.; Contardi, L.; Gianolini, S.; Defossé, G.E. Effects of Canopy Cover and Neighboring Vegetation on the Early Development of Planted Austrocedrus Chilensis and Nothofagus Dombeyi in North Patagonian Degraded Forests. *For. Ecol. Manag.* **2021**, *479*, 118543. [CrossRef]
6. Schumacher, J.; Christiansen, J.R. Forest Canopy Water Fluxes Can Be Estimated Using Canopy Structure Metrics Derived from Airborne Light Detection and Ranging (LiDAR). *Agric. For. Meteorol.* **2015**, *203*, 131–141. [CrossRef]
7. Narine, L.L.; Popescu, S.; Neuenschwander, A.; Zhou, T.; Srinivasan, S.; Harbeck, K. Estimating Aboveground Biomass and Forest Canopy Cover with Simulated ICESat-2 Data. *Remote Sens. Environ.* **2019**, *224*, 1–11. [CrossRef]
8. Næsset, E.; McRoberts, R.E.; Pekkarinen, A.; Saatchi, S.; Santoro, M.; Trier, Ø.D.; Zahabu, E.; Gobakken, T. Use of Local and Global Maps of Forest Canopy Height and Aboveground Biomass to Enhance Local Estimates of Biomass in Miombo Woodlands in Tanzania. *Int. J. Appl. Earth Obs. Geoinf.* **2020**, *93*, 102138. [CrossRef]
9. Parmehr, E.G.; Amati, M.; Taylor, E.J.; Livesley, S.J. Estimation of Urban Tree Canopy Cover Using Random Point Sampling and Remote Sensing Methods. *Urban For. Urban Green.* **2016**, *20*, 160–171. [CrossRef]

10. Hadi; Korhonen, L.; Hovi, A.; Rönnholm, P.; Rautiainen, M. The Accuracy of Large-Area Forest Canopy Cover Estimation Using Landsat in Boreal Region. *Int. J. Appl. Earth Obs. Geoinf.* **2016**, *53*, 118–127. [CrossRef]
11. Jin, X.; Li, Z.; Feng, H.; Ren, Z.; Li, S. Estimation of Maize Yield by Assimilating Biomass and Canopy Cover Derived from Hyperspectral Data into the AquaCrop Model. *Agric. Water Manag.* **2020**, *227*, 105846. [CrossRef]
12. Wolter, P.T.; Townsend, P.A.; Sturtevant, B.R. Estimation of Forest Structural Parameters Using 5 and 10 Meter SPOT-5 Satellite Data. *Remote Sens. Environ.* **2009**, *113*, 2019–2036. [CrossRef]
13. Chen, G.; Lou, T.; Jing, W.; Wang, Z. Sparkpr: An Efficient Parallel Inversion of Forest Canopy Closure. *IEEE Access* **2019**, *7*, 135949–135956. [CrossRef]
14. Liu, S.S.; Chen, D.H.; Li, S.X.; Liu, C.F.; Li, H. Quantitative estimation of stand closure density of Larix sibirica by remote sensing based on GF-1 PMS. *J. Northwest A F Univ. (Nat. Sci. Edi.)* **2020**, *48*, 57–66.
15. Korhonen, L.; Korpela, I.; Heiskanen, J.; Maltamo, M. Airborne Discrete-Return LIDAR Data in the Estimation of Vertical Canopy Cover, Angular Canopy Closure and Leaf Area Index. *Remote Sens. Environ.* **2011**, *115*, 1065–1080. [CrossRef]
16. Halperin, J.; LeMay, V.; Coops, N.; Verchot, L.; Marshall, P.; Lochhead, K. Canopy Cover Estimation in Miombo Woodlands of Zambia: Comparison of Landsat 8 OLI versus RapidEye Imagery Using Parametric, Nonparametric, and Semiparametric Methods. *Remote Sens. Environ.* **2016**, *179*, 170–182. [CrossRef]
17. Li, J.; Mao, X. Comparison of Canopy Closure Estimation of Plantations Using Parametric, Semi-Parametric, and Non-Parametric Models Based on GF-1 Remote Sensing Images. *Forests* **2020**, *11*, 597. [CrossRef]
18. Sun, S.; Li, Z.; Tian, X.; Gao, Z.; Wang, C.; Gu, C. Forest Canopy Closure Estimation in Greater Khingan Forest Based on Gf-2 Data. In Proceedings of the IGARSS 2019—2019 IEEE International Geoscience and Remote Sensing Symposium, Yokohama, Japan, 28 July–2 August 2019; IEEE: Piscataway, NJ, USA, 2019; pp. 6640–6643.
19. Wang, C.; Du, H.Q.; Zhou, G.M.; Xu, X.J.; Sun, S.B.; Gao, G.L. Retrieval of crown closure of moso bamboo forest using unmanned aerial vehicle (UAV) remotely sensed imagery based on geometric-optical model. *Chin. J. Appl. Ecol.* **2015**, *26*, 1501–1509.
20. Tian, H.; Cao, C.; Bao, D.; Dang, Y.; Xu, M. Temporal Changing Analysis of Forest Crown Closure of Anshan City Based on Spectral Mixture Analysis. In Proceedings of the 2013 IEEE International Geoscience and Remote Sensing Symposium—IGARSS, Melbourne, Australia, 21–26 July 2013; IEEE: Piscataway, NJ, USA, 2013; pp. 3809–3812.
21. Kang, Y.; Meng, Q.; Liu, M.; Zou, Y.; Wang, X. Crop Classification Based on Red Edge Features Analysis of GF-6 WFV Data. *Sensors* **2021**, *21*, 4328. [CrossRef]
22. Kim, H.-O.; Yeom, J.-M. Effect of Red-Edge and Texture Features for Object-Based Paddy Rice Crop Classification Using RapidEye Multi-Spectral Satellite Image Data. *Int. J. Remote Sens.* **2014**, *35*, 7046–7068. [CrossRef]
23. Forkuor, G.; Dimobe, K.; Serme, I.; Tondoh, J.E. Landsat-8 vs. Sentinel-2: Examining the Added Value of Sentinel-2's Red-Edge Bands to Land-Use and Land-Cover Mapping in Burkina Faso. *GIScience Remote Sens.* **2018**, *55*, 331–354. [CrossRef]
24. Kaplan, G.; Avdan, U. Evaluating the Utilization of the Red Edge and Radar Bands from Sentinel Sensors for Wetland Classification. *CATENA* **2019**, *178*, 109–119. [CrossRef]
25. Griffiths, P.; Nendel, C.; Hostert, P. Intra-Annual Reflectance Composites from Sentinel-2 and Landsat for National-Scale Crop and Land Cover Mapping. *Remote Sens. Environ.* **2019**, *220*, 135–151. [CrossRef]
26. Ren, H.; Zhou, G.; Zhang, X. Estimation of Green Aboveground Biomass of Desert Steppe in Inner Mongolia Based on Red-Edge Reflectance Curve Area Method. *Biosyst. Eng.* **2011**, *109*, 385–395. [CrossRef]
27. Adam, E.M.I.; Mutanga, O. *Estimation of High Density Wetland Biomass: Combining Regression Model with Vegetation Index Developed from Worldview-2 Imagery*; Neale, C.M.U., Maltese, A., Eds.; International Society for Optics and Photonics: Edinburgh, UK, 2012; p. 85310V.
28. Sibanda, M.; Mutanga, O.; Rouget, M.; Kumar, L. Estimating Biomass of Native Grass Grown under Complex Management Treatments Using WorldView-3 Spectral Derivatives. *Remote Sens.* **2017**, *9*, 55. [CrossRef]
29. Sun, Y.; Qin, Q.; Ren, H.; Zhang, T.; Chen, S. Red-Edge Band Vegetation Indices for Leaf Area Index Estimation From Sentinel-2/MSI Imagery. *IEEE Trans. Geosci. Remote Sens.* **2020**, *58*, 826–840. [CrossRef]
30. Pu, R.; Gong, P.; Biging, G.S.; Larrieu, M.R. Extraction of Red Edge Optical Parameters from Hyperion Data for Estimation of Forest Leaf Area Index. *IEEE Trans. Geosci. Remote Sens.* **2003**, *41*, 916–921. [CrossRef]
31. Shamsoddini, A.; Raval, S. Mapping Red Edge-Based Vegetation Health Indicators Using Landsat TM Data for Australian Native Vegetation Cover. *Earth Sci. Inform.* **2018**, *11*, 545–552. [CrossRef]
32. Adelabu, S.; Mutanga, O.; Adam, E. Evaluating the Impact of Red-Edge Band from Rapideye Image for Classifying Insect Defoliation Levels. *ISPRS J. Photogramm. Remote Sens.* **2014**, *95*, 34–41. [CrossRef]
33. Lin, S.; Li, J.; Liu, Q.; Li, L.; Zhao, J.; Yu, W. Evaluating the Effectiveness of Using Vegetation Indices Based on Red-Edge Reflectance from Sentinel-2 to Estimate Gross Primary Productivity. *Remote Sens.* **2019**, *11*, 1303. [CrossRef]
34. Gara, T.W.; Murwira, A.; Ndaimani, H. Predicting Forest Carbon Stocks from High Resolution Satellite Data in Dry Forests of Zimbabwe: Exploring the Effect of the Red-Edge Band in Forest Carbon Stocks Estimation. *Geocarto Int.* **2016**, *31*, 176–192. [CrossRef]
35. Waśniewski, A.; Hościło, A.; Zagajewski, B.; Moukétou-Tarazewicz, D. Assessment of Sentinel-2 Satellite Images and Random Forest Classifier for Rainforest Mapping in Gabon. *Forests* **2020**, *11*, 941. [CrossRef]

36. Dong, T.; Liu, J.; Qian, B.; He, L.; Liu, J.; Wang, R.; Jing, Q.; Champagne, C.; McNairn, H.; Powers, J.; et al. Estimating Crop Biomass Using Leaf Area Index Derived from Landsat 8 and Sentinel-2 Data. *ISPRS J. Photogramm. Remote Sens.* **2020**, *168*, 236–250. [CrossRef]
37. Astola, H.; Häme, T.; Sirro, L.; Molinier, M.; Kilpi, J. Comparison of Sentinel-2 and Landsat 8 Imagery for Forest Variable Prediction in Boreal Region. *Remote Sens. Environ.* **2019**, *223*, 257–273. [CrossRef]
38. Lee, A.H.; Fung, W.K. Confirmation of Multiple Outliers in Generalized Linear and Nonlinear Regressions. *Comput. Stat. Data Anal.* **1997**, *25*, 55–65. [CrossRef]
39. Verger, A.; Baret, F.; Camacho, F. Optimal Modalities for Radiative Transfer-Neural Network Estimation of Canopy Biophysical Characteristics: Evaluation over an Agricultural Area with CHRIS/PROBA Observations. *Remote Sens. Environ.* **2011**, *115*, 415–426. [CrossRef]
40. Chen, G.; Wulder, M.A.; White, J.C.; Hilker, T.; Coops, N.C. Lidar Calibration and Validation for Geometric-Optical Modeling with Landsat Imagery. *Remote Sens. Environ.* **2012**, *124*, 384–393. [CrossRef]
41. Gemmell, F. An Investigation of Terrain Effects on the Inversion of a Forest Reflectance Model. *Remote Sens. Environ.* **1998**, *65*, 155–169. [CrossRef]
42. Wolf, A.; Berry, J.A.; Asner, G.P. Allometric Constraints on Sources of Variability in Multi-Angle Reflectance Measurements. *Remote Sens. Environ.* **2010**, *114*, 1205–1219. [CrossRef]
43. Franklin, J.; Duncan, J. Testing the Li-Strahler Four-Component Canopy Reflec Rance Model in The Hapex-Sahel Shrub Savanna Sites Using Ground Reflectance Data. In Proceedings of the [Proceedings] IGARSS '92 International Geoscience and Remote Sensing Symposium, Houston, TX, USA, 26–29 May 1992; IEEE: Piscataway, NJ, USA, 1992; pp. 200–202.
44. Peddle, D. Spectral Mixture Analysis and Geometric-Optical Reflectance Modeling of Boreal Forest Biophysical Structure. *Remote Sens. Environ.* **1999**, *67*, 288–297. [CrossRef]
45. Wu, J.; Gao, Z.; Liu, Q.; Li, Z.; Zhong, B. Methods for Sandy Land Detection Based on Multispectral Remote Sensing Data. *Geoderma* **2018**, *316*, 89–99. [CrossRef]